

An 8-Channel Transceiver Coil for Carotid Artery Imaging at 7T using an Optimized Shield Design

Pedram Yazdanbakhsh, Marcus Couch, Kyle M. Gilbert, Johnny Der Hovagimian, David A. Rudko, Richard D. Hoge

Abstract

Objective: To design and fabricate a transmit/receive (T/R) radiofrequency (RF) coil array for MRI of the carotid arteries at 7 T with optimal shielding to improve transmit performance in parallel transmit (pTx) mode.

Methods: The carotid coil included 8 total RF elements, with left and right subarrays, each consisting of 4 overlapping loops with RF shields. Electromagnetic (EM) simulations were performed to optimize and improve the transmit performance of the array by determining the optimal distance between the RF shield and each subarray. EM simulations were further used to calculate local specific absorption rate (SAR) matrices. Based on the SAR matrices, virtual observation points (VOPs) were applied to ensure safety during parallel transmission. The efficacy of the coil design was evaluated by measuring coil performance metrics when imaging a phantom and by acquiring *in-vivo* images.

Results: The optimal distance between the RF shield and each subarray was determined to be 45 mm. This resulted in a maximum B_1^+ efficiency of $1.23 \mu\text{T}/\sqrt{W}$ in the carotid arteries and a peak, 10-g-average SAR per Watt of 0.86 kg^{-1} when transmitting in the nominal CP⁺ mode. Optimizing the RF shield resulted in up to 37% improvement in B_1^+ efficiency and 14% improvement in SAR efficiency compared to an unshielded design.

Conclusion and significance: Optimizing the distance between the RF shield and coil array provided significant improvement in the transmit characteristics of the bilateral carotid coil. The bilateral coil topology provides a compelling platform for imaging the carotid arteries with high field MRI.

Index Terms: *Phased Array RF coil, High-field MRI, 7 Tesla, Parallel transmission, Carotid imaging*

Date of submission: August 1, 2023. This project was funded by HBHL Core Facilities (250075), the Canadian Institutes of Health Research (MOP-123492), the Canadian Foundation for Innovation (JELF 34874 and Innovation Fund 33397), Brain Canada in Partnership with Health Canada (PSG15-3755) and the Canada First Research Excellence Fund (HBHL-4b-CF-10).

*P. Yazdanbakhsh is with McConnell Brain Imaging Centre, Montreal Neurological Institute and Hospital, McGill University, Montreal, QC, Canada and Department of Neurology and Neurosurgery, McGill University, Montreal, QC, Canada (correspondence e-mail: pedram.yazdanbakhsh@mcgill.ca).

M. Couch is with McConnell Brain Imaging Centre, Montreal Neurological Institute and Hospital, McGill University, Montreal, QC, Canada, Department of Neurology and Neurosurgery, McGill University, Montreal, QC, Canada and Siemens Healthcare Limited, Montreal, QC, Canada

K. M. Gilbert is with Centre for Functional and Metabolic Mapping, Western University, London, ON, Canada.

I. INTRODUCTION

High-resolution vascular imaging represents one of the most exciting applications at 7 Tesla. The increased sensitivity [1], [2] and higher parallel imaging acceleration factors [3], [4] achievable at 7 T can be leveraged to resolve the human carotid artery bifurcation [5]. The carotid artery bifurcation has a high rate of plaques [6], [7]; therefore, imaging of this structure is important for diagnosing and monitoring many vascular diseases like Takayasu's arteritis [8]. The potential utility of 7 T carotid artery imaging has previously been demonstrated [9], [10].

Simultaneous mapping of the two carotids offers numerous advantages. These include practical benefits such as higher throughput and efficiency, improved patient comfort, consistency of image quality, and more efficient use of contrast agents. For advanced research applications, this capability allows techniques such as quantification of whole-brain blood flow using phase-contrast velocity encoding over all major vessels in the neck.

The full potential of carotid imaging can only be realized with coils optimized for the targeted anatomy. The application of surface RF coils and phased arrays [11] can produce the requisite SNR to identify atherosclerotic plaques in the carotid arteries. This is notably true at ultra-high field. Since whole-body transmit coils are not available on 7 T MR systems due to the high required power and large B_1 field inhomogeneity [12], it is necessary to design either a transceiver coil for both RF transmit and receive or independent transmit and receive coils.

J. D. Der Hovagimian was with McConnell Brain Imaging Centre, Montreal Neurological Institute and Hospital, McGill University, Montreal, QC, Canada and Department of Biomedical Engineering, McGill University, Montreal, QC, Canada. He is now with AEM Antennas Inc., Montreal, QC, Canada.

D.A. Rudko is with McConnell Brain Imaging Centre, Montreal Neurological Institute and Hospital, McGill University, Montreal, QC, Canada, Department of Neurology and Neurosurgery, McGill University, Montreal, QC, Canada and Department of Biomedical Engineering, McGill University, Montreal, QC, Canada.

R. D. Hoge is with McConnell Brain Imaging Centre, Montreal Neurological Institute and Hospital, McGill University, Montreal, QC, Canada, Department of Neurology and Neurosurgery, McGill University, Montreal, QC, Canada and Department of Biomedical Engineering, McGill University, Montreal, QC, Canada

Earlier studies specifically showed the benefits of designing a 7 T transmit/receive (T/R) carotid array to allow parallel imaging, as well as to facilitate simultaneous mapping of both carotid arteries for a side-by-side comparison [13], [14]. While SNR increases with the static magnetic field $|B_0|$ [15], [16], commensurate increases in SAR and B_1^+ inhomogeneity are expected due to decreasing the wavelength of the electromagnetic field inside the human body.

Many different methods have been used to solve these problems at 7T, such as the use of a conventional RF shield. The RF shield can decouple the RF and gradient coils [17]. The RF shield can also help to prevent radiation losses and signal wrapping from unwanted regions [18], [19]. To increase the B_1 -efficiency/improve the B_1 -homogeneity and decrease the SAR, it is essential to optimize the distance between the RF-shield and the RF coil [20], [21]. Optimal design of conductive shielding is crucial for achieving the best performance from multi-channel RF coils, especially for MRI scanners operating at high magnetic fields. As the adoption of 7 Tesla MRI systems increases, along with the commercial availability of clinically approved scanners, this aspect of coil design has become increasingly important.

In this work, we focus on imaging the human carotid artery at 7 T using parallel transmission (pTx).

We show that by optimizing the radiofrequency shield of an 8-channel T/R carotid coil array, we can simultaneously optimize both B_1^+ -efficiency and SAR at the location of the left and right carotid arteries.

Decoupling of the coil was performed geometrically with an optimum overlap and by including an optimized RF shield.

The coil array was evaluated using a series of RF performance metrics with varying load conditions. Human imaging demonstrated the bilateral phased array was capable of producing high-resolution images of the carotids.

II. METHODS

A. Coil Design and Construction

An 8-channel T/R carotid coil array was designed and built for a 7T Siemens MAGNETOM Terra whole body MRI scanner operating in parallel transmission (pTx) mode. Eight parallel transmitters were used to drive the array in pTx mode.

The coil consists of eight T/R array elements and an interface box.

Each side of the coil (left/right) was comprised of four overlapped loops [see Fig. 1(a)] and an RF shield [see Fig. 1(b)]. The RF shield was slotted and bridged with 680-pF capacitors (ATC, 100B) to mitigate eddy currents.

The dimension of each loop was 80 mm x 90 mm with a copper thickness of 30 μm . Each loop was etched onto an FR4 laminate material with 0.8-mm thickness. Four overlapped loops had a length of 190 mm and a width of 115 mm with an overlap of 9 mm between the loops [see Fig. 2].

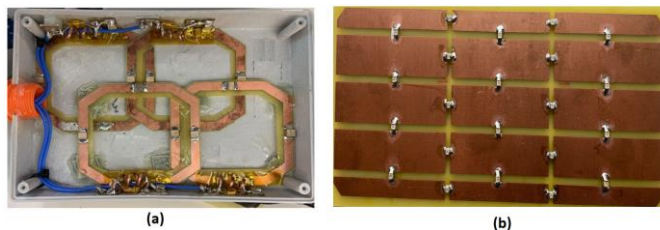


Fig. 1. Each side of the carotid coil (a) four overlapped loops designed to be positioned on each side of the neck. (b) The RF shield incorporated on each side with 680-pF capacitors to mitigate eddy currents

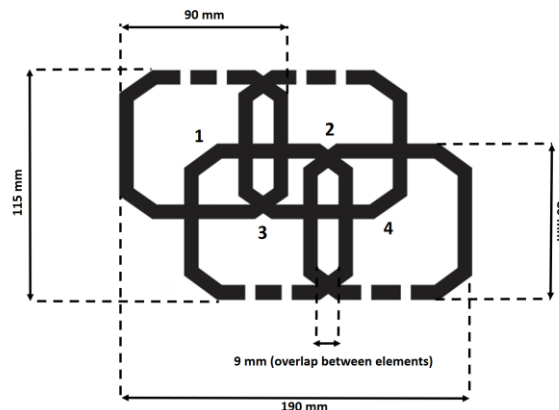


Fig. 2. Schematic and dimension of each of the four elements applied for the carotid artery coil. An overlap of 9 mm existed between the loop elements

Three 7-pF, high-power non-magnetic capacitors (ATC, 100C) and two 14-pF capacitors (ATC, 100C) were incorporated into each loop. Each loop's input port consisted of a cable trap and a 15-pF matching capacitor (ATC, 100C). The cable traps were formed by a 4-cm long, semi-rigid coaxial cable (Pasternack, PECX005) wound into four turns in parallel with an 8-pF high-power capacitor (ATC, 100C). Each set of four overlapped shielded loops was geometrically optimized to minimize the mutual coupling between elements.

Each element was resonated at the 7 T ^1H Larmor resonance frequency of 297.2 MHz (specific to the Siemens 7T scanner) and matched to 50 Ω . Tuning and matching for each element, as well as the mutual coupling between elements, was optimized on the bench when the coil was loaded with a 7-L plastic bottle Siemens phantom (Length=37cm, diameter=15cm, per 1000g distilled water: 3,75g $\text{NiSO}_4 \cdot 6 \text{H}_2\text{O}$ + 5g NaCl) and a SAM Head phantom (SPEAG, Switzerland, SAM-V4.5) with the same geometry as the human head/neck. Tuning and matching was also carried out using the neck of a 24-year-old healthy human (male) volunteer on the bench. S-parameter measurements were performed using a network analyzer (KEYSIGHT E5061B). Finally, S-parameters and loaded/unloaded quality factors ($Q_{\text{unloaded}}/Q_{\text{loaded}}$) were determined for all coil elements.

The interface box (shown in Fig. 3) was comprised of eight quarter-wavelength ($\lambda/4$) T/R switches [22], with RF chokes, to allow switching between transmit and receive mode of the RF coil. Fig. 4(a) shows the circuit diagram of the $\lambda/4$ T/R switch for alternating between transmit and receive mode. Each T/R switch was connected to a WanTcom preamplifier (part number# WMM7RP) for signal amplification.

To tune the preamplifier decoupling, a phase shifter was included at the input port of each preamplifier.

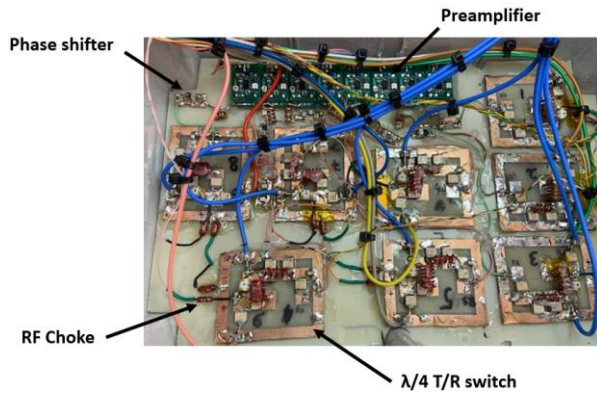


Fig. 3. The interface box consisting of 8 transmit/receive switches with RF chokes, 8 preamplifiers, and 8 phase shifters.

Fig. 4(b) shows the circuit diagram of Pi phase shifters used before preamplifiers for preamplifier decoupling. Fig. 4(c) shows the circuit diagram of each RF loop with associated cable trap, T/R switch, phase shifter and preamplifier. **TABLE I** Shows the component values and detailed information regarding circuit components for each loop and the RF chain.

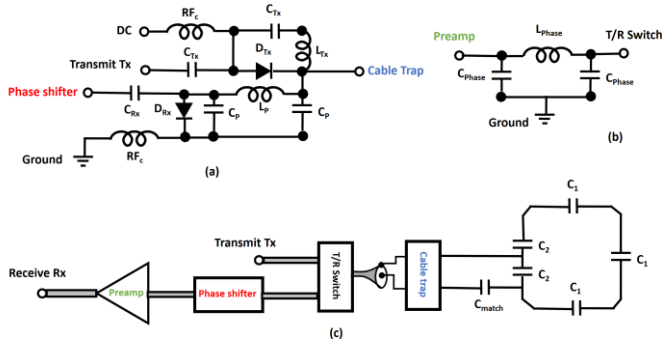


Fig. 4. Circuit diagram of a T/R switch, phase shifter and loop (a) $\lambda/4$ T/R switch (b) Pi phase shifter used before each preamplifier and (c) The circuit diagram of each loop with associated cable trap, T/R switch, phase shifter and preamplifier.

B. Simulations

EM Simulations were performed using CST Studio Suite (Dessault Systemes, SIMULIA, Minnesota, USA, CST Studio Suite 2020) using Finite-Integration-Technique (FIT) method to guide geometric aspects of the coil design. The simulations were also applied to assess the SAR characteristics of the coil to ensure patient safety. This was done in two steps:

Step 1) Before fabricating the coil: (i) to optimize dimensions of each loop and the overlap distance, and (ii) to optimize the distance between the RF shield and the loops on each side of the neck to minimize the mutual coupling between loops, minimize the SAR per Watt, and maximize the B_1^+ efficiency, all while the coil was loaded with the CST's Gustav body model (38 years old, male, 176 cm, 69 kg, Number of tissues: 33,

TABLE I
COMPONENT INFORMATION AND DETAILED COMPONENT VALUES FOR THE CIRCUIT DIAGRAM SHOWN IN FIG. 4

Symbol	Component	Value	Used in
RF_c	RF Choke (Jahre, 71.10-1R00K)	$1\mu\text{H}$	T/R switch
C_{TX}	Capacitor (ATC, 100C)	680pF	T/R switch
L_{TX}	Homemade Inductor	180nH	T/R switch
D_{TX}	Pin Diode (MACOM, MA4PK2000)	----	T/R switch
L_P	Inductor (Coilcraft, 1008CS)	27nH	T/R switch
C_P	Capacitor (ATC, 100B)	10.5pF	T/R switch
D_{RX}	Pin Diode (MACOM, MA4PK2000, MA4P7470F-1072T)	----	T/R switch
L_{Phase}	Inductor (Coilcraft, 1008CS)	25nH	LC phase shifter
C_{Phase}	Capacitor (ATC, 100B)	15.3pF	LC phase shifter
C_1	Capacitor (ATC, 100C)	7pF	Each loop
C_2	Capacitor (ATC, 100C)	14pF	Each loop
C_{match}	Capacitor (ATC, 100C)	15pF	Each loop

Resolution: $2.08 \times 2.08 \times 2 \text{ mm}^3$. Minimum mesh cell size (Fraction of maximum cell near to model): 20, Nx: 503, Ny: 338, Nz: 440, Largest cell: 14.66, smallest cell: 0.74, Number of cells: 74,267,386. Boundaries: open (add space).

Step 2) After fabricating the coil: to ensure robust patient safety when operating the carotid coil in pTx mode, local SAR matrices were derived and validated using the method outlined by Gilbert et al. [23]. Commensurate virtual observation points (VOPs) were also calculated for online SAR supervision [24] in MATLAB (The Mathworks, Natick, MA, USA). A safety factor of 1.8 was added to VOPs as an extra precaution to ensure patient safety [25], [26].

C. Parallel Transmit (pTx)

To achieve an optimized B_1^+ excitation vector for RF excitation, the phase for each individual transmit (Tx) channel was optimized in two stages: (1) CST-derived channel-specific, B_1^+ maps were imported into MATLAB, then combined through complex addition of individual maps weighted by an input phase vector. The optimal phase vector was determined by

minimizing the coefficient of variation (CV) of the combined B_1^+ map. The CV was evaluated by placing two rectangular regions of interest (ROIs) near the right and left subarrays. (2) A B_1^+ map was then acquired on the scanner for each individual Tx channel using the simulation-derived optimal phases. The B_1^+ maps were experimentally acquired using a Siemens-provided saturation-prepared Turbo-FLASH B_1^+ mapping sequence. This phase optimization was then repeated in MATLAB using the experimentally-derived B_1^+ maps. The goal of the phase optimization was to minimize the CV of the channel-combined B_1^+ maps. The final phase vector was then entered into the coil files for use in all subsequent phantom and *in vivo* imaging.

D. Imaging

After constructing the coil [see Fig. 5] and performing detailed workbench tests, phantom images were acquired in two stages. First, imaging of a phantom was performed using Turbo-FLASH B_1^+ mapping sequence with the calculated VOP files to measure B_1^+ excitation uniformity in the phantom. Second, representative magnitude images were collected for validating the coil performance in standard imaging. These images were acquired using a 2D spoiled gradient echo sequence (TE = 10 ms, TR = 100ms, FOV= 300 x 300 mm², BW= 260 Hz/Px, Matrix size= 128 x 128, FA = 25°, Slices = 1, Slice thickness: 5 mm, t_{acq} = 14 s) and a 2D spin echo sequence (TE = 15 ms, TR = 300ms, FOV= 300 x 300 mm², BW= 130 Hz/Px, Matrix size= 128 x 128, FA = 25°, Slices = 1, Slice thickness: 5 mm, t_{acq} = 80 s). Additionally, a noise correlation matrix was calculated from a noise-only scan on the 7 T human MRI system.

Following the validation of the EM SAR models using EM simulations and phantom imaging, the carotid arteries of three healthy volunteers were scanned using the 7 T MRI system at the Montreal Neurological Institute of McGill University. All volunteers gave informed consent for the imaging procedures. The imaging tests were approved under McGill HREB protocol # 2021-6129. For *in vivo* imaging of blood flow in the arteries, a 3D phase contrast (PC) angiography sequence was applied (TE = 6 ms, TR = 43 ms, FOV= 162 x 200 mm², BW= 500 Hz/Px, Matrix size= 260 x 320, FA = 12°, Slices = 192, Slice thickness: 0.5 mm, t_{acq} = 9 min, v_{enc} = 75 cm/s). As well, a 3D time-of-flight (TOF) sequence (TE/TR= 3.4/18ms, FOV= 181 x 200 mm², BW= 1860 Hz/Px, Matrix size= 331 x 384, FA = 24°, Slices = 256, Slice thickness: 0.5 mm, t_{acq} = 6 min) was used for bright-blood imaging of the full left and right carotid arteries.



Fig. 5. The constructed 8-channel transmit-receive carotid coil

III. RESULTS

A. Workbench testing

TABLE II shows the S-parameters and Q-ratio values when the coil was loaded with the SAM phantom.

The reflection coefficients (S_{ii}) for all channels at 297.2 MHz when the coil was loaded with SAM phantom, 7-L standard Siemens phantom, and human neck were all lower than -20 dB. The transmission coefficients (S_{ij}) between any two channels of the carotid array were all lower than -15 dB. These S_{ii} and S_{ij} measurements were taken with the optimized shield, before preamplifier decoupling [27].

TABLE II
S-PARAMETERS AND Q-RATIO VALUES

Channel	S_{ii}	S_{ij} / other channels (worst case)	Q_{un}/Q_L
1	-20 dB	-15 dB	2
2	-21 dB	-17 dB	1.96
3	-20 dB	-16 dB	2.17
4	-23 dB	-16 dB	2.38
5	-23 dB	-16 dB	2.1
6	-20 dB	-16 dB	2.21
7	-22 dB	-17 dB	2.1
8	-22 dB	-16 dB	2.23

The quality-factor ratio for all channels was better than 1.96 for all three loading conditions. This ratio and the Q-ratio values in TABLE II were measured for each element in the presence of all other channels when the coil was used with fixed tuning and matching capacitors. When a single element was used alone and retuned to 297.2 MHz (unloaded case), the Q-ratio without a matching capacitor was better than 3.8 for all three loading conditions.

Preamplifier decoupling was implemented with 110-degree Pi phase shifters at the input of each preamplifier.

Fig. 6(b) shows the measured S_{21} for one channel using a dual probe and vector network analyzer [see Fig. 6(a)], while the preamplifier was powered on with 10 V. Like Fig. 6(b), all other channels had the same minimum at 297.2 MHz. The standard deviation for the preamplifier decoupling values for all channels was 0.44.

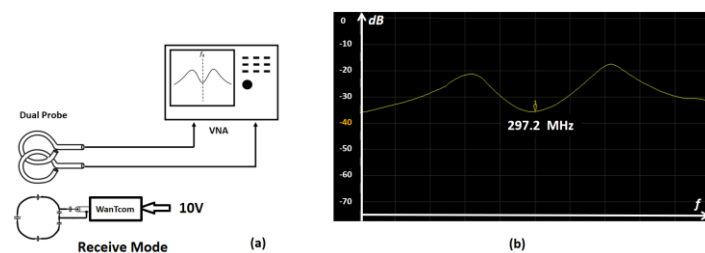


Fig. 6. Workbench testing (a) Dual probe and vector network analyzer (VNA) for preamplifier decoupling. For measurements, the dual probe was connected to both ports of the VNA and 10 V was applied to the preamplifier. (b) Measured S_{21} for one channel after preamplifier decoupling

B. EM simulations and Imaging

1) EM simulations before fabricating the coil

EM simulations were employed to optimize the RF transceiver loop position and the loop overlap. For this purpose, both the positions and the mutual overlap of all four elements on each side of the coil were progressively shifted and the mutual coupling between elements were recorded. This was first done without considering the presence of any RF shield.

The worst-case mutual coupling between the four elements without the RF shield was found to be -12 dB when the coil was loaded with the “Gustav” body model [see Fig. 7].

Next, to consider the impact of the RF shield on coil element coupling, the distance between the RF shield and the loops on each side of the neck was adjusted. In particular, the RF shield was shifted in position from a point 5 mm away (very proximal) from the RF loops to a point 60 mm from the loops, in order to examine the mutual coupling between the elements at each shield position.

Fig. 8 shows the worst-case mutual coupling between RF transceiver elements in the carotid coil as a function of the distance between the RF shield and the array. The minimum worst-case mutual coupling between the four elements was -17dB. This was the case when the distance between the RF shield and array was 40 mm - 45 mm. This optimized coupling (S_{21}) was 5 dB better than this array without an RF shield.

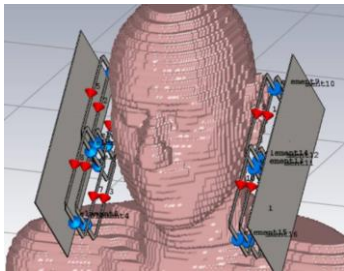


Fig. 7. EM simulation for the array using the Gustav body model (38 years old, male, 176 cm, 69 kg, Number of tissues: 33)

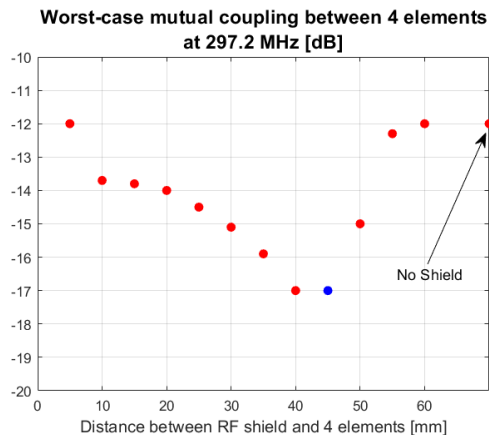


Fig. 8. EM simulation for the array using the Gustav body model to find the effect of the RF shield on the worst-case mutual coupling between all elements

To minimize the maximum 10-g-average SAR per Watt in the circular polarized (CP⁺) mode of the coil, the distance between the RF shield and the RF elements was again varied between 5 mm and 60 mm and the SAR was simulated. The CP⁺ mode was achieved by driving the top loops (loops 1 and 2) in Fig. 2 with a 0° phase and the bottom loops (loops 3 and 4) with a 180° phase, while maintaining a constant RF amplitude for all channels. To simplify the analysis, a constant excitation vector was used that produced the theoretical CP⁺ mode.

Fig. 9 shows the maximum 10-g-average SAR per Watt in CP⁺ mode in the carotid artery by varying the distance between the RF shield and elements.

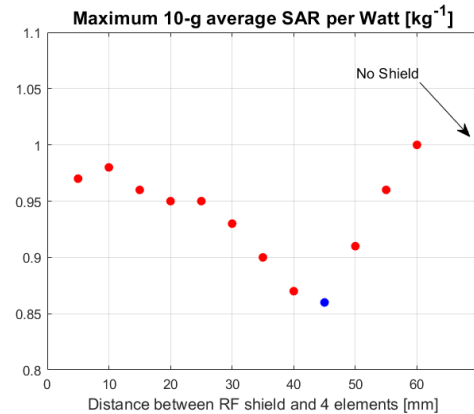


Fig. 9. EM simulation for the array using the Gustav body model to find the effect of the RF shield on the maximum 10-g average SAR per Watt for the eight channel carotid coil in CP⁺ mode

The minimum “max 10-g-average SAR per Watt” in CP⁺ mode was 0.86 kg⁻¹ when the distance between the RF shield and array was 45 mm. This optimized “maximum 10-g-average SAR per Watt” was 14% better than this array without an RF shield.

Finally, to maximize the B₁⁺ efficiency [$\mu T/\sqrt{W}$] of all 8 elements when transmitting in CP⁺ mode, the distance between the RF shield and elements was again varied between 5 mm and 60 mm. Fig. 10 shows the B₁⁺ efficiencies of all 8 elements as a function of the distance between the RF shield and the RF transceiver elements.

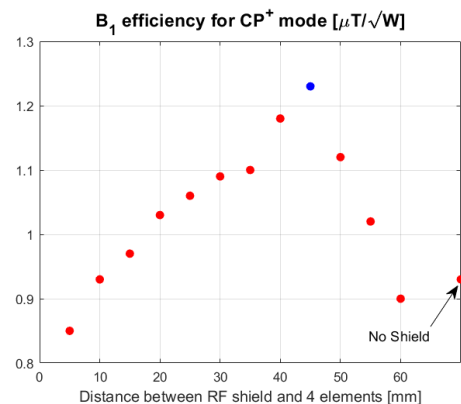


Fig. 10. EM simulation for the array using the Gustav body model to find the effect of the RF shield on B₁⁺-efficiency of the eight-channel carotid coil in CP⁺ mode

The maximum B_1^+ efficiency in CP⁺ mode was found to be 1.23 $\mu\text{T}/\sqrt{W}$ in the carotid artery ROI when the distance between the RF shield and array was 45mm. This optimized B_1^+ efficiency is 37% better than the B_1^+ efficiency of this array without an RF shield.

For the results in Fig. 8, Fig. 9 and Fig. 10, both the tune and match of each channel were readjusted after changing the distance between the RF shield and elements. The goal was to have a resonance frequency of 297.2 MHz with S_{ii} better than -15 dB after changing and shifting the RF shield. Collectively considering the results in these figures, the distance between the RF shield and elements was chosen to be 45 mm

Results of the EM simulations displaying B_1^+ efficiency and SAR distribution within the CST anatomical Gustav model are shown in Fig. 11 when both the left and right RF shields are at the optimal distance of 45mm from the coil. B_1^+ simulations were carried out with the nominal CP⁺ transmit mode. The maximum B_1^+ efficiency in the carotid artery was 1.23 $\mu\text{T}/\sqrt{W}$ and the maximum 10-g-average SAR was 0.86 W.kg^{-1} when transmitting in CP⁺ mode. Simulations have been normalized to 1W of accepted power.

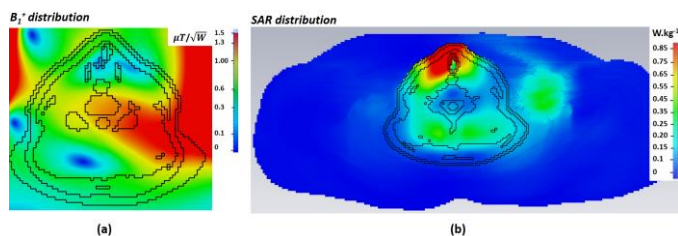


Fig. 11. EM Simulation results for the eight-channel carotid coil driven in CP⁺ mode and loaded with the Gustav human model. Simulations have been normalized to 1W of accepted input power (a) 2D B_1^+ distribution for the axial plane (b) 2D SAR distribution for the axial plane

2) EM simulations and imaging after fabricating the coil

After optimizing the coil array using EM simulation and fabricating the coil, the optimized pTx excitation vector was determined. B_1^+ maps were exported from EM simulations assuming the coil was loaded with the standard 7-L Siemens phantom. Fig. 12 (top row) shows a central slice B_1^+ map before and after optimizing the phases using simulated data. The optimized map shows a reduced CV of simulated B_1^+ over the ROIs near the right and left sub-arrays. The simulation-optimized phases were then used as a starting point for optimizing phases again in experimental B_1^+ maps. Fig. 12 (bottom row) shows the initial B_1^+ map acquired on the scanner using the same phantom and the optimized phases from Stage 1, followed by the final predicted B_1^+ map after minimizing the CV of the experimental B_1^+ over the similar ROIs near the right and left sub-arrays.

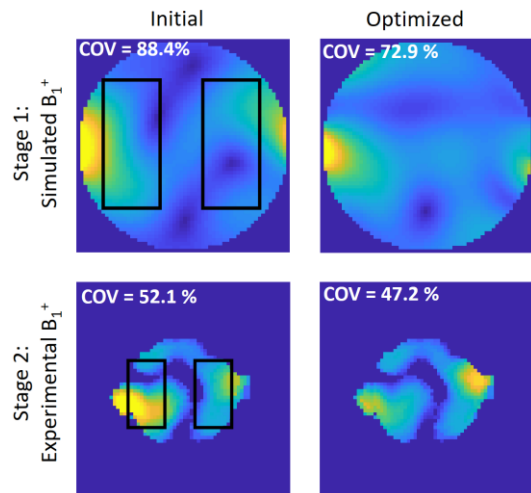


Fig. 12. Optimizing pTx excitation vector. (Top row) Stage 1 optimization using simulated B_1^+ maps, with black boxes indicating the chosen ROIs for coefficient of variation (CV) evaluation. (Bottom row) Stage 2 optimization using the Stage 1 phases as a starting point.

TABLE III shows the maximum 10-g-average SAR normalized to 1W of accepted power using the Gustav model for the three scenarios: Nominal CP⁺, Stage 1, and Stage 2.

TABLE III
10-G-AVERAGE SAR FOR THREE SCENARIOS

Scenario	SAR (W.kg^{-1})
Nominal CP ⁺	0.86
Stage 1	0.91
Stage 2	0.94

The excitation phases can in principle be optimized on experimental data only. We chose to include an initial phase optimized on simulated data to provide a reasonable first guess for acquiring experimental B_1 maps. TABLE IV shows the phase adjustments implemented on each channel to produce the optimized B_1^+ in Stage 1 and Stage 2. The amplitude was $1/\sqrt{8}$ for each channel.

TABLE IV
PHASE ADJUSTMENTS FOR THE OPTIMIZED B_1^+ IN BOTH STAGES

Channel	Stage 1	Stage 2
1	-91	-75
2	43	94
3	38	49
4	-61	-19
5	167	-169
6	-10	-6
7	145	124
8	36	-11

After optimizing the design, local SAR matrices and virtual observation points (VOPs) were then calculated for online SAR supervision. To validate the SAR models, another set of B_1^+ maps were acquired in the phantom using the final phases from

Stage 2 of the excitation vector optimization.

Fig. 13 shows a comparison of the simulated and experimental B_1^+ maps at an individual channel level. The complex simulated B_1^+ maps were scaled and phase matched, as described in Gilbert et al. [23]. Differences in B_1^+ between experimental and simulated data can be attributed to losses and phase changes not accounted for in simulation, such as those caused by cabling and T/R switches. Fig. 14 shows experimental and simulated B_1^+ maps combined using the optimized excitation vector.

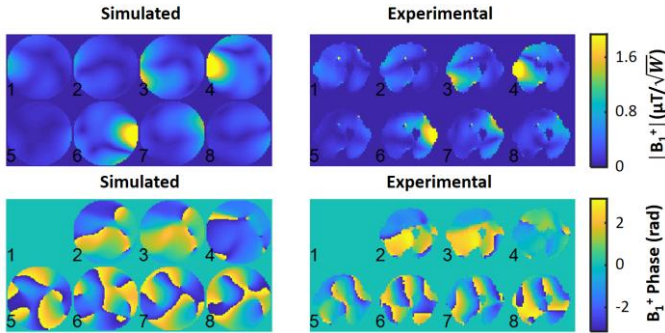


Fig. 13. Simulated and experimental B_1^+ -maps (magnitude and phase) for individual channels of the carotid array when loaded with the standard 7-L Siemens phantom. B_1^+ phase images were calculated by subtracting the phase of the first channel.

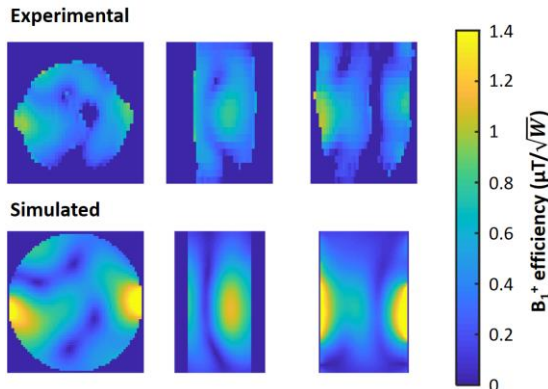


Fig. 14. Simulated and experimental B_1^+ efficiency maps for the nominal CP⁺ driving mode. For the experimental case, the coil was loaded with the standard 7-L Siemens phantom

The receiver performance was evaluated in part through phantom scanning. Fig. 15(a) shows a gradient-echo image of the standard 7-L Siemens phantom acquired when receivers were combined. Fig. 15(b) shows the receiver combined (adaptive combination) image from a 2D spin echo sequence when using the SAM phantom as the load.

Fig. 15(c) shows the calculated receiver noise correlation matrix. The mean noise correlation was 21% when the standard 7-L Siemens phantom was used.

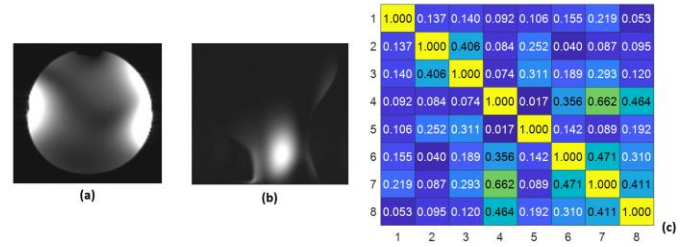


Fig. 15. MR phantom images and noise correlation matrix (a) Sagittal gradient-echo image of all 8 channels combined using the 7-L standard Siemens Phantom for loading, (b) Receiver combined image from 2D spin echo using the SAM phantom and (c) The noise correlation matrix for the carotid coil

Image quality was subsequently assessed *in-vivo*. Fig. 16 display 3D phase contrast (PC) angiography and 3D time-of-flight (TOF) images in a human volunteer taken after optimizing the RF transmit phase and amplitude of each channel to achieve maximum B_1^+ homogeneity. Fig. 17 shows both carotid arteries of the 24-year-old healthy human (male) subject imaged using 3D Time-of-Flight (TOF) sequence.

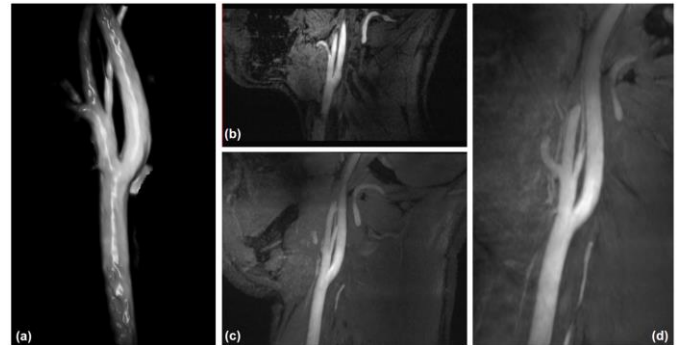


Fig. 16. MR *in-vivo* images (a) 3D phase contrast (PC) angiography. (b), (c) and (d) 3D time-of-flight (TOF) images of a 24-year-old healthy subject

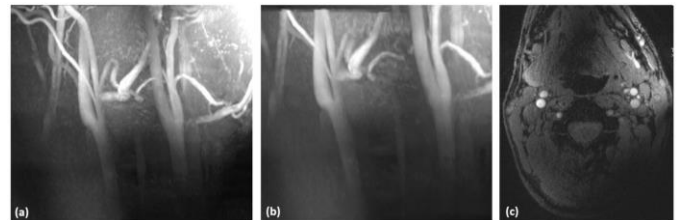


Fig. 17. Magnitude images of the carotid arteries of a 24-year-old healthy subject acquired using a 3D TOF MR acquisition with TR=18ms and TE=3.4ms (a) oblique image with 2 averages, (b) oblique image with 1 average and (c) axial image of the carotid arteries

IV. DISCUSSION AND CONCLUSIONS

An 8-channel transceiver, carotid artery coil with four channels on each side of the neck was designed and constructed for high resolution, 7 T imaging of the carotid bifurcation. The coil integrated a custom, slotted RF shield on each side of the neck. The distance between the RF shield and RF transmit array elements was optimized, resulting in improved SAR performance and B_1^+ efficiency compared to an unshielded design. By simulating the SAR matrices and calculating the

final VOP matrix, the coil was used for parallel transmission with SAR values within patient safety limits.

In vivo imaging experiments demonstrated that, with an optimized excitation vector, there is sufficient B_1^+ efficiency and SNR for high resolution imaging of both the left and right carotid arteries.

Our coil used fixed capacitors instead of variable capacitors for tuning and matching of each element. The advantage of using fixed capacitors is that it procures tuning and matching stability over long scans. Variable capacitors may drift in value over long scans. While variable capacitors could provide flexibility to optimize the tuning and matching for different neck sizes, such a step is time consuming and typically not practical for human, *in vivo* imaging.

The T/R carotid coil designed in this work used a rigid former geometry rather than a flexible substrate (for example, mounted inside foam). With a rigid design, the RF shield distance could be optimized and fixed. Such a step would be difficult to do using a flexible design. One of the challenges encountered with the proposed carotid coil design was adapting the coil array to small necks. In future designs, this could be done by engineering an alternative, flexible array.

Since adjusting the phase on each transmit element is a popular method to create an improved B_1^+ pattern over the ROI [28]-[30], the carotid coil was specifically constructed to operate in parallel transmission (pTx) mode. pTx operation gives the flexibility to optimize the amplitude and phase of each channel (B_1^+ -shimming). This allows improved transmit field homogeneity.

Our work, in this regard, focused on optimizing the initial excitation vector, by adjusting only the phase of the input vector. This optimized excitation vector produced a reasonable B_1^+ homogeneity near the right and left carotid arteries. Due to the target ROI placement during phase optimization, some destructive interference of signal was expected at the center of the phantom or subject. These signal voids, however, are not expected to impact imaging of the carotids, However, they could be mitigated in future by using more advanced B_1^+ shimming algorithms such as multi-slice B_1^+ shimming or by using 3D RF pulses. An advantage of our approach, however, is its ease of implementation since B_1^+ -shims for our study were optimized online for each subject in less than 1 minute.

The transmit architecture presented in this work could also be applied in a multi-coil approach at 7T to perform arterial spin-labeling, which must have excellent coverage of both carotid and vertebral arteries and has been challenging due to the transmit limitations of available head coils.

In summary, the 8-channel, 7 T coil design presented in this work provided high-resolution MR images of both the left and right carotid arteries with sufficient penetration depth for exciting blood signals.

ACKNOWLEDGMENT

This project was funded by HBHL Core Facilities (250075), the Canadian Institutes of Health Research (MOP-123492), the Canadian Foundation for Innovation (JELF 34874 and Innovation Fund 33397), Brain Canada in Partnership with Health Canada (PSG15-3755) and the Canada First Research Excellence Fund (HBHL-4b-CF-10). Research Support from Siemens Healthineers Limited is gratefully acknowledged. We thank Mr. David Costa for his valuable support as an MR technologist during the human MRI scans conducted in this study.

REFERENCES

- [1] M. E. Ladd, "High-field-strength magnetic resonance: potential and limits," *Top Magn Reson Imaging*. 2007; 18:139–152.
- [2] J. F. Schenck, E. A. Zimmerman, "High-field magnetic resonance imaging of brain iron: birth of a biomarker," *NMR Biomed*. 2004; 17:433–445.
- [3] O. Dietrich, "General Advantages of Parallel Imaging," *Parallel Imaging in Clinical MR Applications*. Medical Radiology. Springer, Berlin, Heidelberg. https://doi.org/10.1007/978-3-540-68879-2_16
- [4] S. Moeller, et al., "Multiband multislice GE-EPI at 7 tesla, with 16-fold acceleration using partial parallel imaging with application to high spatial and temporal whole-brain fMRI," *Magn Reson Med*. 2010; 63:1144-53.
- [5] C. Yuan, et al., "MRI of carotid atherosclerosis," *J. Nucl. Cardiol*. 2008; 15: 266–275.
- [6] S. Carr, et al., "Atherosclerotic plaque rupture in symptomatic carotid artery stenosis" *J. Vasc Surg*. 1996; 23:755–766.
- [7] H. S. Bassiouny, et al., "Critical carotid stenoses: morphologic and chemical similarity between symptomatic and asymptomatic plaques" *J. Vasc Surg*. 1989; 9:202–212.
- [8] B. Trinidad, et al., "Takayasu Arteritis" *StatPearls [Internet]*. Treasure Island (FL): StatPearls Publishing; 2023 Jan-. Available: <https://www.ncbi.nlm.nih.gov/books/NBK459127/>
- [9] M. Piccirelli, N. DeZanche, J. Nordmeyer-Massner, et al., "Carotid artery imaging at 7T: SNR improvements using anatomically tailored surface coils" *Proceedings 16th Scientific Meeting, International Society for Magnetic Resonance in Medicine*; April 2008; Toronto, Ontario, Canada.
- [10] G. Wiggins, et al., "7 Tesla transmit-receive array for carotid imaging: simulation and experiment" *Proceedings 17th*

Scientific Meeting, International Society for Magnetic Resonance in Medicine; April 2009; Honolulu, HI.

[11] C. E. Hayes, et al., "Surface coil phased arrays for high resolution imaging of the carotid arteries" *J Magn Reson Imaging*. 1996; 6: 109–112.

[12] S. Orzada, et al., "A 32-channel parallel transmit system add-on for 7T MRI" *PLOS ONE*. 14. e0222452. 10.1371/journal.pone.0222452.

[13] O. Kraff, et al., "A Transmit/Receive Radiofrequency Array for Imaging the Carotid Arteries at 7 Tesla" *Investigative Radiology*; Volume 46, Number 4, April 2011

[14] T. Ruytenberg T, et al., "A flexible five-channel shielded-coaxialcable (SCC) transceive neck coil for high-resolution carotid imaging at 7T" *Magn Reson Med*. 2020; 84: 1672–1677.

[15] D. I. Hoult, "The principle of reciprocity in signal strength calculations - A mathematical guide," *Concepts in Magnetic Resonance*. 2000; 12:173-187.

[16] J. T. Vaughan, M. Garwood, C. M. Collins et al., "7T vs. 4T: RF power, homogeneity, and signal-to-noise comparison in head images," *Magn Reson Med*. 2001 ;46:24-30.

[17] C. E. Hayes and M. G. Eash, "Shield for decoupling RF and gradient coils in an NMR apparatus," *US Patent 4642569*. 1987.

[18] S. Handa, T. Haishi, K. Kose, "Development of a local electromagnetic shielding for an extremity magnetic resonance imaging sys-tem," *Rev Sci Instrum*. 2008; 79:113706.

[19] P. E. Van Hecke, et al., "Use of shielding to prevent folding in MR imaging," *Radiology*. 1988; 167:557-558.

[20] P. Yazdanbakhsh, et al., "An 8-Channel Transceive Head Coil Array for 7T," *ESMRMB 2013, Toulouse, France, 2013*.

[21] B. Zhang, et al., "Effect of radiofrequency shield diameter on signal-to-noise ratio at ultra-high field MRI," *Magn Reson Med*. 2021; 85:3522–3530.

[22] C. N. Chen, et al., "Biomedical magnetic resonance technology", *Institute of Physics Publishing, Bristol and Philadelphia, 1989*

[23] K. M. Gilbert, et al., "Radiofrequency coil for routine ultra-high-field imaging with an unobstructed visual field" *NMR Biomed*. 2021; 34: e4457

[24] G. Eichfelder, M. Gebhardt, "Local specific absorption rate control for parallel transmission by virtual observation points" *Magn Reson Med*. 2011; 66: 1468–76.

[25] E. F. Meliado, et al., "Intersubject specific absorption rate variability analysis through construction of 23 realistic

body models for prostate imaging at 7T" *Magn Reson Med*. 2019; 81:2106-2119.

[26] M. Le Garrec, et al., "Probabilistic analysis of the specific absorption rate intersubject variability safety factor in parallel transmission MRI" *Magn Reson Med*. 2017;78:1217-1223.

[27] P. B. Roemer, et al., "The NMR phased array" *Magn Reson Med*. 1990; 16:192–225.

[28] G. J. Metzger, et al., "Local B_1^+ shimming for prostate imaging with transceiver arrays at 7T based on subject-dependent transmit phase measurements" *Magn Reson Med*. 2008; 59:396-409.

[29] V. Pfaffenrot, et al., "An 8/15-channel Tx/Rx head neck RF coil combination with region-specific B_1^+ shimming for whole-brain MRI focused on the cerebellum at 7T" *Magn Reson Med*. 2018; 80:1252-1265.

[30] C. Sun C, et al., "A retrofit to enable dynamic B_1^+ steering for transmit arrays without multiple amplifiers" *Magn Reson Med*. 2021; 85:3497-3509.